

This document is the Accepted Manuscript version of a Published Work that appeared in final form in Nano Letters, © 2023 American Chemical Society after peer review and technical editing by the publisher.

To access the final edited and published work see <https://pubs.acs.org/doi/10.1021/acs.nanolett.2c03913>.

How do Quantum Effects Influence the Capacitance and Carrier Density of Monolayer MoS₂ Transistors?

Robert K. A. Bennett¹ and Eric Pop^{1,*}

¹*Department of Electrical Engineering, Stanford University, Stanford, California 94305, U.S.A.*

*Contact: epop@stanford.edu

ABSTRACT: When transistor gate insulators have nanometer-scale equivalent oxide thickness (EOT), the gate capacitance (C_G) becomes smaller than the oxide capacitance (C_{ox}) due to the quantum capacitance and charge centroid capacitance of the channel. Here, we study the capacitance of monolayer MoS₂ as a prototypical two-dimensional (2D) channel while considering spatial variations in the potential, charge density, and density of states. At 0.5 nm EOT, the monolayer MoS₂ capacitance is smaller than its quantum capacitance, limiting the single-gated C_G of an n -type channel to between 63% and 78% of C_{ox} for gate overdrive voltages between 0.5 and 1 V. Despite these limitations, for dual-gated devices, the on-state C_G of monolayer MoS₂ is 50% greater than that of silicon at 0.5 nm EOT and more than three times that of InGaAs at 1 nm EOT, indicating that 2D semiconductors are promising for nanoscale devices at future technology nodes.

KEYWORDS: Semiconductor capacitance, quantum capacitance, centroid capacitance, electrostatics, field-effect transistor, 2D semiconductor

Two-dimensional (2D) semiconductors have emerged over the last decade as promising candidates for channel materials in sub-10-nm metal-oxide-semiconductor field-effect transistors (MOSFETs).^{1,2} Using 2D monolayer semiconductors in such transistors is appealing from an electrostatic perspective because their ultrathin channel (< 1 nm) reduces the impact of lateral fringing fields while increasing the 2D semiconductor's out-of-plane capacitance C_{sc} (sometimes called the inversion layer capacitance in bulk semiconductor transistors in the on-state). Although conventional bulk semiconductors (like silicon) suffer from mobility degradation as their channel thickness is reduced to a few nanometers, 2D semiconductors maintain good carrier mobilities even at their monolayer limit, allowing them to simultaneously offer excellent electrostatic control and good on-state conductance.^{3,4}

In a field-effect transistor, the total gate capacitance $C_G = q\partial n_{ch}/\partial V_G$ [where q is the elementary charge, n_{ch} is the number of charge carriers (electrons or holes) per unit area, and V_G is the gate voltage] is given by the series capacitance of C_{sc} with the gate insulator capacitance, denoted here as C_{ox} (acknowledging that gate insulators may have nitrides or other components),^{5,6} as shown in Figure 1a and equation 1:

$$\frac{1}{C_G} = \frac{1}{C_{sc}} + \frac{1}{C_{ox}}. \quad (1)$$

The semiconductor channel's contribution to C_G is negligible when $C_{sc} \gg C_{ox}$, at which point $C_G \approx C_{ox} = \epsilon_{ox}/t_{ox}$, where ϵ_{ox} and t_{ox} are the insulator's permittivity and thickness, respectively. If C_{sc} is comparable to C_{ox} , however, then C_{sc} can limit C_G , thereby limiting the maximum carrier densities achievable in the FET on-state.⁵ For example, we demonstrate in this work that for monolayer MoS₂, C_{sc} is negligible when the gate insulator's equivalent oxide thickness (EOT) is ≥ 2.5 nm, although the precise EOT at which C_{sc} becomes negligible varies between semiconductors.^{5,7-9}

The C_{sc} has two main components: the centroid capacitance (due to the penetration of the charge centroid into the semiconductor channel^{5,10}) and the quantum capacitance C_q (due to Fermi level movement with respect to the energy bands in a semiconductor channel with finite density of states^{9,11-13}). For 2D semiconductors, the centroid capacitance has often been taken as infinite (implicitly assuming $C_{sc} \approx C_q$), where C_q is evaluated as¹²

$$C_q = 2\pi \frac{q^2 g_s g_v m^*}{h^2} \left(1 + \frac{\exp[E_G/(2k_B T)]}{2 \cosh[q\psi_{ch}/(k_B T)]} \right)^{-1}, \quad (2)$$

where $g_s = 2$ is the spin degeneracy, g_v is the valley degeneracy ($= 2$ and 6 for the lower K-valleys and the higher Q-valleys, respectively, of the conduction band in monolayer MoS₂), m^* is the effective mass, h is Planck's constant, E_G is the electronic band gap (≈ 2.2 eV for monolayer MoS₂, depending on its dielectric environment¹⁴), k_B is the Boltzmann constant, and T is the absolute temperature (here, ~ 300 K). Above, ψ_{ch} is the channel potential, typically considered without regard to its variation in the channel of 2D semiconductors (i.e., infinite centroid capacitance) but self-consistently treated in this work with spatial variation of charge density. Although C_q is very small in the off-state, in the on-state a large $|\psi_{ch}|$ pushes the Fermi energy into the channel conduction or valence bands, causing the bracketed term in equation (2) to approach unity and saturating C_q to its degenerate value C_{dq} , given by^{12,15}

$$C_{dq} = 2\pi \frac{q^2 g_s g_v m^*}{h^2}. \quad (3)$$

Considering only the lowest-energy conduction and valence bands, $C_{dq} \approx 70$ and $200 \mu\text{F}/\text{cm}^2$ for n - and p -type monolayer MoS_2 , respectively. Although including higher energy bands (e.g., the Q-valley along the T-line¹⁶ in the monolayer MoS_2 conduction bands) would enable larger C_q , even these lower-bound estimates of C_{dq} greatly exceed C_{ox} for any realistic EOT, leading most studies to neglect C_{sc} .

However, previous experimental studies on monolayer semiconductors, including MoS_2 , MoSe_2 , WSe_2 , and black phosphorus, have reported values of C_q and C_{sc} that are much smaller than their respective C_{dq} when the Fermi energy E_F is pushed beyond the band edges.¹⁷⁻¹⁹ Although these smaller-than-anticipated capacitances could be attributed to extrinsic contributions (like defects), recent theoretical work has shown that for monolayer MoS_2 , other components of C_{sc} could limit it to values much smaller than C_{dq} .²⁰ However, the contribution of non-uniform carrier distributions across a 2D semiconductor's thickness, as well as the impact that this reduced C_{sc} will have on C_G , remain largely unexplored.

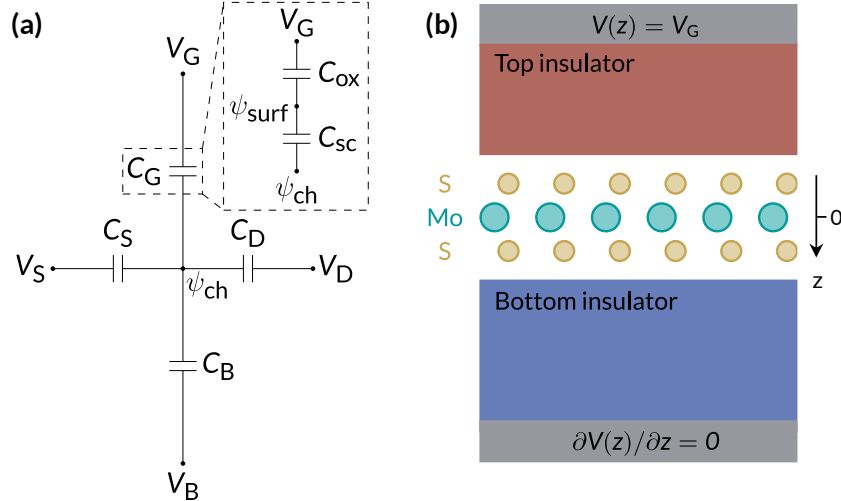


Figure 1. (a) Capacitance network model of a 2D transistor. C and V represent capacitances and potentials, subscripts G, S, D, and B denote quantities associated with the gate, source, drain, and the bottom insulator/substrate, respectively. ψ_{ch} is the channel potential, which can vary across the thickness of the channel. The inset shows C_G as the series capacitance of C_{ox} and C_{sc} with an intermediate surface potential ψ_{surf} . (b) Schematic of the MoS_2 -based MOS capacitor considered in this work, along with boundary conditions applied when solving equations (4) and (5).

In this work, we address these gaps in knowledge by self-consistently solving carrier statistics equations with the electrostatic potential distribution across a monolayer MoS_2 -based MOS capacitor, as shown in Figure 1b. We consider the spatial variation of electrostatic potential $V(z)$ [where z is the cross-plane coordinate labeled in Figure 1b], the volumetric charge density $\rho(z)$, and the local density of states (LDOS)^{21,22} across the monolayer thickness, and we write

$$\rho(z) = \mp q \int \text{LDOS}(E, z) \left[\frac{1}{2} \mp \frac{1}{2} \pm f(E) \right] dE \quad (4)$$

where E is the energy, $f(E)$ is the Fermi-Dirac distribution, upper (lower) signs are for electrons (holes), and the channel carrier density n_{ch} is obtained by integrating $|\rho(z)|/q$. Applying a gate voltage changes $\rho(z)$ and n_{ch} by modulating the local electrostatic potential $V(z)$, pushing E_{F} from mid-gap towards the conduction (valence) bands and populating the channel with electrons (holes).

Here, we assume that the intrinsic semiconductor E_{F} is at the mid-gap energy, allowing us to equate E_{F} with $qV(z)$ when computing $f(E)$ in equation (4), where $qV(z)$ is also referenced to mid-gap. As both $\rho(z)$ and $V(z)$ are unknowns, we solve equation (4) self-consistently with Poisson's equation,

$$\frac{\partial}{\partial z} \left[\epsilon(z) \frac{\partial V}{\partial z} \right] = -\rho(z), \quad (5)$$

where $\epsilon(z)$ is the permittivity. We discretize $V(z)$ and $\rho(z)$ along a one-dimensional grid, including the gate voltage boundary condition [$V(z) = V_{\text{G}}$] at the top of the gate insulator and a Neumann boundary condition [$\partial V(z)/\partial z = 0$] at the opposite side of the bottom insulator in the structure shown in Figure 1b.

We model $\epsilon(z)$ as a step-like function that transitions from ϵ_{ox} to the MoS₂ permittivity¹⁷ $4\epsilon_0$ (where ϵ_0 is the permittivity of vacuum) at $z = -t_{\text{ch}}/2$, then to the permittivity of SiO₂ ($3.9\epsilon_0$) at $z = t_{\text{ch}}/2$, where $t_{\text{ch}} = 0.615$ nm is the MoS₂ monolayer thickness. We note that this dielectric profile is approximate; many different estimates for the out-of-plane dielectric constant of monolayer MoS₂ have been reported,^{4,17,23,24} and it is unclear how $\epsilon(z)$ varies spatially at the insulator/MoS₂ interface. Furthermore, it is uncertain if $\epsilon(z)$ is mostly constant across the thickness of the MoS₂ monolayer or if, like graphene,²⁵ $\epsilon(z)$ is a function of position within the monolayer. Once these factors are known, they can be incorporated into our model by substituting the appropriate dielectric profile into equation (5).

We extract the LDOS of monolayer MoS₂ using density functional theory (DFT) with Quantum ESPRESSO software.²⁶ All calculations are performed on a $151 \times 151 \times 1$ k -point grid using projector-augmented wave pseudopotentials with kinetic energy cutoffs of 60 Ry for wave functions and 480 Ry for charge densities and potentials. After computing the LDOS for a primitive cell in three dimensions, we average the LDOS across the in-plane directions to represent it only as functions of E and z . Then, to ensure that the LDOS at a specific energy will always sum to the magnitude of the DOS at that same energy, we express it as

$$\text{LDOS}(E, z) = L(E, z)\text{DOS}(E), \quad (6)$$

where $L(E, z)$ is the spatial distribution of the LDOS,²¹ which we normalize at each energy level E_n :

$$L(E = E_n, z) = \frac{\text{LDOS}(E=E_n, z)}{\int_{-\infty}^{\infty} \text{LDOS}(E=E_n, z) dz}. \quad (7)$$

Figures 2a,b show $L(E, z)$ in the conduction and valence bands, respectively. At $E \leq E_{\text{C}} + 0.25$ eV (where E_{C} is the conduction band minimum), the LDOS is confined close to the center of the MoS₂ monolayer (i.e., near the Mo atoms) with sharp, narrow peaks appearing just to the left and right of the main central peak. These sharp satellite peaks arise from the spatial distribution of the $4d_{z^2}$ orbital of Mo, which has

been shown to dominate the DOS at these energies in previous studies.^{27,28} Furthermore, we find that broad peaks centered close to the S atoms appear in the LDOS at $E > E_C + 0.25$ eV. As shown in the projected DOS (pDOS) in Figure 2c, the S atoms begin to contribute to the DOS in the conduction bands at ~ 0.26 eV above the conduction band minimum, corresponding to the Q-K valley separation ΔE_{QK} from our DFT simulations. Projected band structures have also shown that S atoms contribute weakly to the electronic structure of monolayer MoS₂ at the conduction band minimum, but they contribute noticeably to the Q-valley.^{27,29} We therefore attribute these peaks to contributions to the DOS from the S atoms.

Similar laterally positioned peaks are present at all values of $E \leq E_V$ (where E_V is the valence band maximum) we consider in Figure 2b, which is also consistent with the pDOS in the valence bands: as shown in Figure 2d, S atoms contribute to the DOS in the valence bands at all considered energies. Similarly, projected band structures have shown that both Mo and S atoms contribute significantly to the valence bands of monolayer MoS₂.^{27,29}

We note that the exact ΔE_{QK} for monolayer MoS₂ in vacuum is not precisely known³⁰ and that the band structure of monolayer MoS₂ can vary depending on strain³¹ and its surrounding dielectric environment.¹⁴ For example, the experimental ΔE_{QK} for monolayer MoS₂ encased in quartz and WS₂ is $\Delta E_{QK} \approx 0.11$ eV,³² and simulated values range between 0.071 and 0.270 eV, depending on the approach used.³⁰ To accommodate this uncertainty in the value of ΔE_{QK} , we investigate its effect on C_{sc} and n_{ch} in Section S1 of the Supporting Information. We also note from Figures 2a,b that the LDOS extends slightly beyond $t_{ch} = 0.615$ nm, which occurs because DFT simulations of 2D MoS₂ assume that the semiconductor is surrounded by vacuum; in reality, a semiconductor's LDOS cannot so easily penetrate into an insulator.³³ However, we shortly demonstrate that this non-ideality should not significantly affect our results.

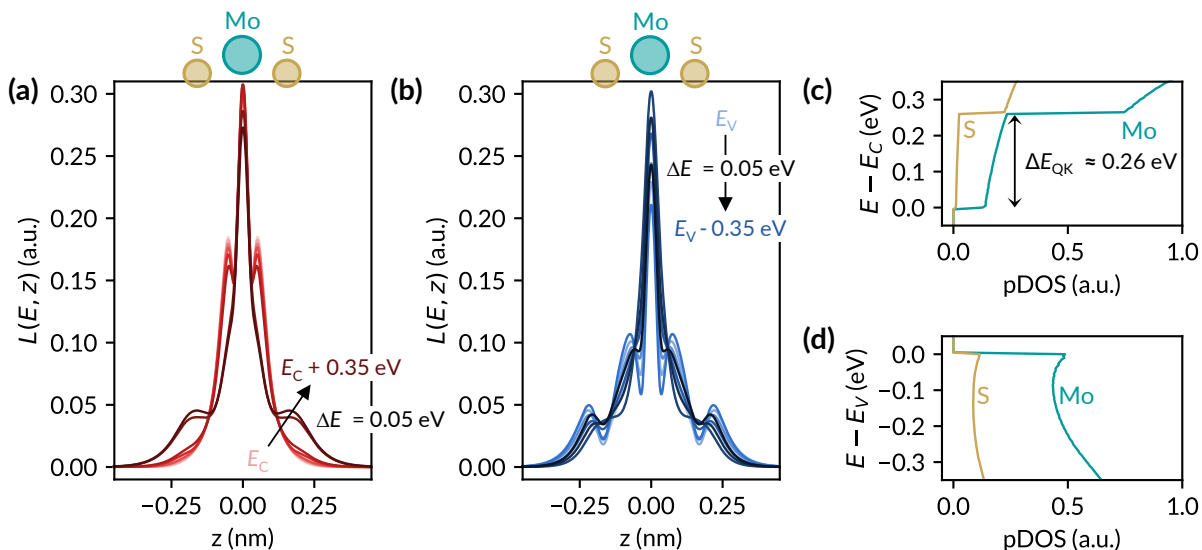


Figure 2. Normalized spatial distribution of the local density of states $L(E, z)$ across monolayer MoS₂ at (a) $E \geq E_C$, and (b) $E \leq E_V$, where the z coordinates of Mo and S atoms align with the location of atoms at the top of the figures (size of atoms are not to scale). Projected density of states (pDOS) for (c) conduction bands and (d) valence bands of monolayer MoS₂, where the contributions of all orbitals from each individual atom are summed together. Note that the contributions from only one S atom are shown in (c) and (d); a.u., arbitrary units.

In Figures 3a,b, we calculate and plot C_{sc} of monolayer MoS₂ on linear and logarithmic y-axes, respectively, by self-consistently solving equations (4) and (5) under an applied gate bias, with the corresponding n_{ch} values plotted in Figure 3c. For now, we set the permittivity of the gate insulator to an extremely large value ($C_{ox} \rightarrow \infty$), so that $\psi_{surf} = V_G$, allowing us to study the intrinsic capacitance of monolayer MoS₂ by neglecting the potential drop across the gate insulator. We will shortly relax this assumption and study monolayer MoS₂-based capacitors with finite EOTs.

At $|\psi_{surf}| - E_G/(2q) < 0.25$ V, the capacitance of *p*-type MoS₂ exceeds that of *n*-type MoS₂, which is due to the DOS near the valence band edge being larger than the DOS near the conduction band edge (Figures 2c,d). However, as ψ_{surf} is pushed farther into the conduction bands, the slopes of both C_{sc} and n_{ch} increase sharply for *n*-type MoS₂. This increase is due to the step-like increase in the DOS at the Q-valley, noting that thermal broadening in equation (4) allows the DOS from the Q-valley to also contribute when E_F is a few $k_B T$ below the edge of the Q-valley. We note that this effect has been experimentally observed in MoSe₂ and WSe₂ monolayers, which have similar electronic structures to that of MoS₂ (including a Q-valley above the conduction band edge). Thus, the shape of the electron density in our Figure 3c resembles similar experimental curves for MoSe₂ and WSe₂ monolayers.¹⁸

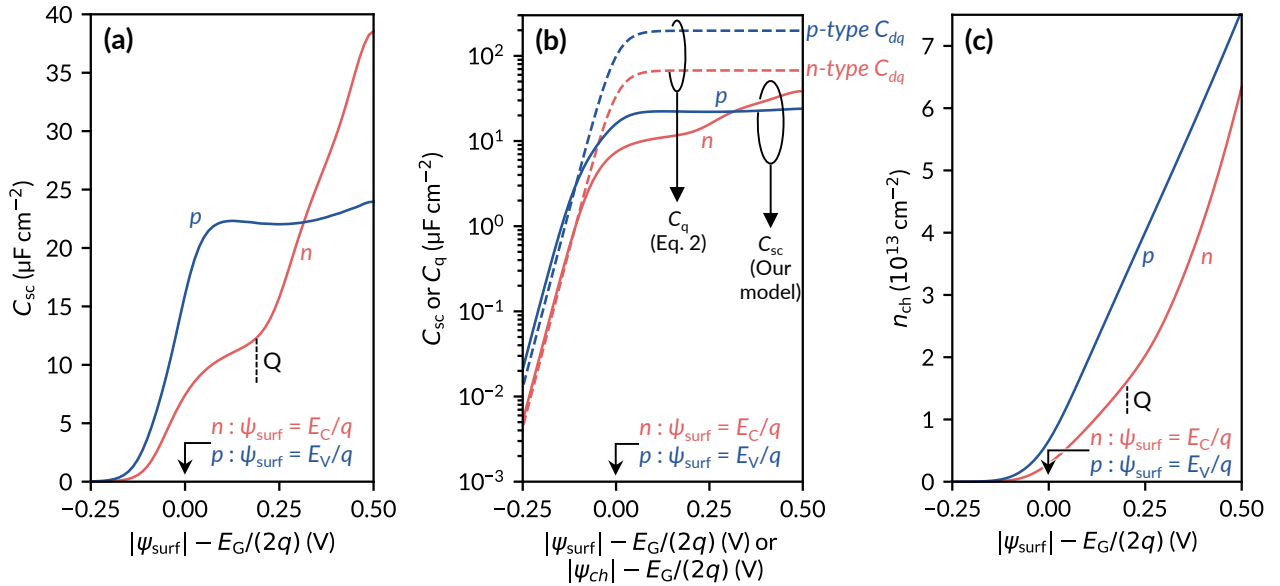


Figure 3. Semiconductor capacitance C_{sc} as a function of $|\psi_{surf}| - E_G/(2q)$ plotted on (a) linear and (b) logarithmic axes. For comparison, we also plot quantum capacitance C_q as a function of the channel potential ψ_{ch} [calculated using equation (2) with $g_{vm}^* = 1.01m_0$ and $2.96m_0$ for electrons and holes,⁴ respectively] in (b). (c) Charge carrier density n_{ch} for *n*-type and *p*-type monolayer MoS₂. The approximate location at which the Q-valley begins to contribute to the capacitance and carrier density of *n*-type monolayer MoS₂ is marked in (a) and (c) with a vertical dashed line. Note, carrier densities over $\sim 2 \times 10^{13} \text{ cm}^{-2}$ are difficult to access in practice with conventional dielectrics (e.g. HfO₂) but can be accessed with solid or liquid electrolyte gating.

We also compare our computed C_{sc} values to the conventional C_q for both n - and p -type monolayer MoS₂, which we have plotted alongside C_{sc} in Figure 3b. Although our calculated C_{sc} closely matches C_q at small gate voltage (i.e., non-degenerate surface potentials), we find that at high gate voltages (i.e., degenerate potentials), our computed C_{sc} values are substantially lower than the traditionally calculated $C_q = C_{dq} = 70 \mu\text{F}/\text{cm}^2$ for n -type and $200 \mu\text{F}/\text{cm}^2$ for p -type monolayer MoS₂, respectively. To understand why C_{sc} matches C_q only for *non-degenerate* potentials, we first plot the charge distributions and potential across the thickness of n -type (p -type) MoS₂ when ψ_{surf} is 0.3 V below (above) the conduction (valence) band edge in Figures 4a,b. For this non-degenerate case, the charge distributions are nearly symmetric across the channel, closely matching the LDOS distributions shown in Figures 2a,b. This result is consistent with the potential profile shown in Figure 4b: there is nearly no potential drop across the monolayer MoS₂ thickness, allowing electronic states to contribute to the carrier density equally efficiently, regardless of their location in the channel. Hence, $C_{sc} \approx C_q$ in this regime.

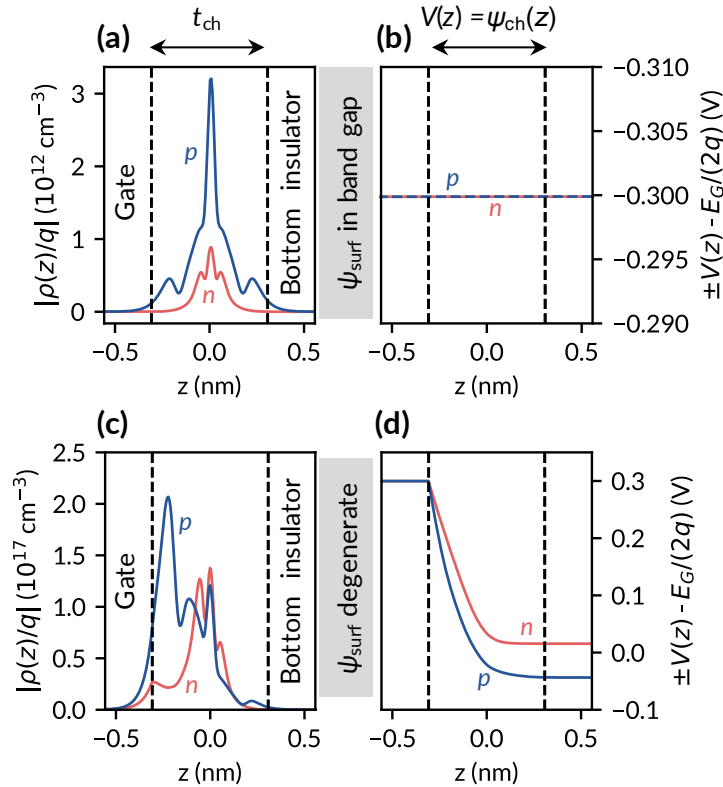


Figure 4. (a) Distributions of charge density and (b) potential profile across the MoS₂ monolayer with ψ_{surf} inside the band gap, 0.3 eV below the conduction band edge (for electrons) and 0.3 eV above the valence band edge (for holes). (c) Distributions of charge density and (d) potential profile across the MoS₂ monolayer with ψ_{surf} of 0.3 eV above the conduction band edge (for electrons) and 0.3 eV below the valence band edge (for holes). Dashed lines indicate boundaries with the gate electrode and bottom insulator. Note, the carrier densities in (c) are much greater than in (a). In (c), the carrier distribution also extends slightly outside t_{ch} by $< 10\%$ of total n_{ch} , meaning that the charge centroid is closer to the gate²⁰ and that C_{sc} is slightly overestimated in this study. Finally, we note that the potential drops are different for n - and p -type devices in Figure 4d because the capacitance of n -type monolayer MoS₂ is smaller than that of p -type MoS₂ for the ψ_{surf} we consider here.³⁴

Next, to understand why $C_{sc} < C_q$ at *degenerate* potentials, we plot the charge distributions and potential across the thickness of monolayer n -type (p -type) MoS₂ when ψ_{surf} is 0.3 V above (below) the conduction (valence) band edge in Figures 4c,d. We find that for this degenerate case, the charge distributions are heavily asymmetric and skewed towards the gate electrode. This asymmetry can be explained from the potential drops in Figure 4d, which shows that the local electrostatic potential is highest near the gate electrode and rapidly decays across the monolayer channel. We recall from Figures 2a,b that most available states are near the center of the channel in this region of relatively low potential. Therefore, many states are unable to efficiently contribute to n_{ch} , which is why $C_{sc} < C_{dq}$ even at high ψ_{surf} . As a result, the charge density is askew across the thickness of the MoS₂ monolayer, with the S atoms opposite to the gate contributing little to the channel charge. We conclude that at degenerate surface potentials, the shapes of the LDOS and potential profile play pivotal roles in dictating C_{sc} for 2D semiconductors.

We next consider the impact of C_{sc} in practical MOS devices based on monolayer MoS₂. Figures 5a,b plot C_G and n_{ch} for MOS capacitors as in Figure 1b with EOTs of 0.5, 1, and 2.5 nm ($\epsilon_{ox} = 20\epsilon_0$). For comparison, we additionally plot $C_{ox} = 3.9\epsilon_0/EOT$, as well as the classical carrier density $n_{ch}^{classical} = (V_G - V_T)C_{ox}/q$ (for electrons; the bracketed term is negated for holes), where the threshold voltage is $V_T = \pm E_G/(2q)$ for n - and p -type devices, assuming the same gate metal. At EOT = 2.5 nm, C_G saturates close to C_{ox} and $n_{ch} \approx n_{ch}^{classical}$, but the observed C_G and n_{ch} deviate significantly from C_{ox} and $n_{ch}^{classical}$, respectively, at EOTs of 0.5 and 1 nm. For example, at EOT = 0.5 nm, the C_G of n -type MoS₂ increases from 4.38 $\mu\text{F}/\text{cm}^2$ at 0.5 V to 5.35 $\mu\text{F}/\text{cm}^2$ at 1 V, remaining between 63% and 78% of C_{ox} . However, we note that C_G is sensitive to small variations in V_G and to the position of the Q-valley for n -type MoS₂, as captured in Figure 5a and discussed in Supporting Information Section S1.

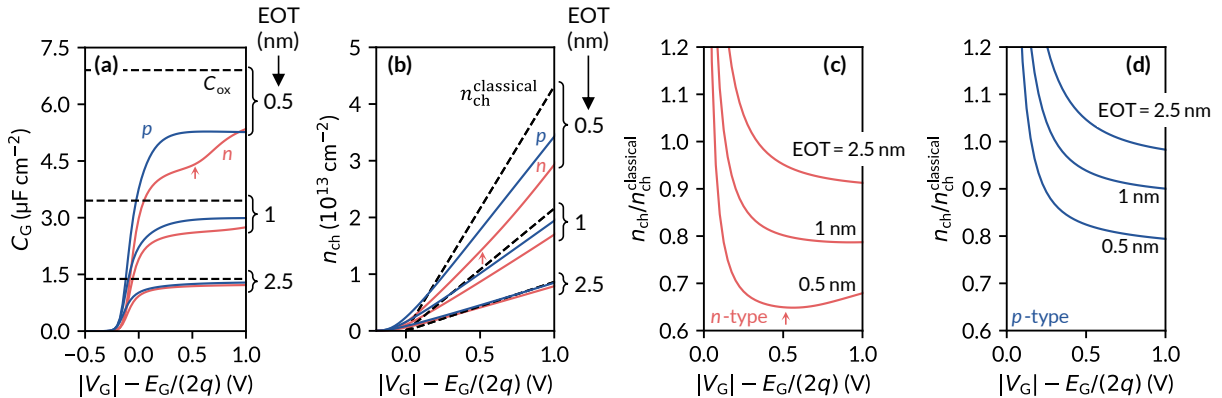


Figure 5. (a) Gate capacitance C_G and (b) charge carrier density n_{ch} for n -type and p -type monolayer MoS₂ as functions of V_G at EOT = 0.5, 1, and 2.5 nm. Solid red (blue) lines represent n -type (p -type) MoS₂. Dashed lines mark the oxide capacitance C_{ox} and the conventionally calculated carrier density $n_{ch}^{classical}$, highlighting the importance of quantum corrections in the limit of ultrathin EOT. Small red arrows mark approximately where the Q-valley of n -type MoS₂ begins to contribute. (c) Calculated $n_{ch}/n_{ch}^{classical}$ for n -type MoS₂ and (d) p -type MoS₂. The true charge density is lower than the classical estimate in the limit of high V_G when transistors are strongly turned on. However, $n_{ch}^{classical}$ approaches zero and underestimates the true charge density near threshold.

Similarly, we find that the classical equation overestimates n_{ch} in 2D MOS capacitors with small EOTs, as shown in Figures 5c,d for n - and p -type MoS₂, respectively. At EOTs of 0.5 and 1 nm, the channel carrier density n_{ch} is as small as 65% and 79% (79% and 89%) of $n_{\text{ch}}^{\text{classical}}$ for n -type (p -type) MoS₂ in the V_G range considered here. We note that contributions from the Q-valley are visible for the n -type device with EOT = 0.5 nm, leading to an increase in C_G and n_{ch} when the voltage is sufficiently high. This effect has also been observed experimentally in ion-gated MoSe₂ and WSe₂ monolayers, which have similar band structures to that of monolayer MoS₂.¹⁸

We note that $n_{\text{ch}}^{\text{classical}} = C_{\text{ox}}(V_G - V_T)/q$ should not be applied near or below V_T , because this expression neglects subthreshold charge.⁶ Instead, n_{ch} may be approximated in both the off- and on-states by taking C_G as the series combination of C_q and C_{ox} ,^{11,12} and then integrating the result (up to the relevant V_G) to find the carrier density. However, as we demonstrate in Section S2 of the Supporting Information, correcting for C_q in this manner still significantly overestimates both C_G and n_{ch} in the on-state for 2D channels with low EOT, highlighting the importance of including both quantum and centroid effects when modeling these devices.

Finally, we assess how C_{sc} limits C_G for monolayer MoS₂ compared to other semiconductors, including silicon. Although decreasing t_{ch} improves the channel electrostatics, $t_{\text{ch}} < 5$ nm causes surface scattering to limit silicon carrier mobilities.^{2,35,36} At the limit $t_{\text{ch}} \approx 5$ nm, a previous study³⁷ has shown that the C_{sc} of silicon limits a dual-gated silicon FET with an EOT of 0.5 nm to $C_G \approx 7 \mu\text{F}/\text{cm}^2$ at an overdrive $V_{\text{OV}} = V_G - V_T = 1$ V. In direct comparison, our calculations show that a similar dual-gated structure with n -type monolayer MoS₂ offers $C_G \approx 10.9 \mu\text{F}/\text{cm}^2$ (10.6 $\mu\text{F}/\text{cm}^2$ for p -type), over 50% greater than that of silicon. The MoS₂ advantage persists even when the silicon thickness is reduced³⁷ to 2.5 nm, which yields $C_G \approx 8.1 \mu\text{F}/\text{cm}^2$. We refer the reader to Section S3 of the Supporting Information for a description of how we calculated C_G and n_{ch} for dual-gated devices and for full C_G and n_{ch} vs. V_G curves.

The C_{sc} of monolayer MoS₂ compares even more favorably to III-V semiconductors, whose low DOS are known to limit their C_q . A previous study³⁸ has shown that C_q limits dual-gated InGaAs MOS capacitors with EOT = 1 nm to $C_G < 1.6 \mu\text{F}/\text{cm}^2$ at channel thickness $t_{\text{ch}} = 25$ nm; as t_{ch} decreases, this C_G worsens because the DOS shrinks due to quantum confinement effects.³⁸ Using the same approach as above, we find that a dual-gated monolayer n -type MoS₂ capacitor with EOT = 1 nm offers $C_G \approx 5.55 \mu\text{F}/\text{cm}^2$ (or 6.00 $\mu\text{F}/\text{cm}^2$ for p -type) at $V_{\text{OV}} = 1$ V, over three times higher than InGaAs. The results from Figure 5a also indicate that single-gated monolayer MoS₂ capacitors with EOT of 2.5 nm offer higher C_G than those reported for single-gated In_{0.7}Ga_{0.3}As and InAs capacitors with similar or lower EOTs.⁵

In conclusion, we have shown that variations in carrier density (i.e., the centroid capacitance), potential, and density of states across the thickness of monolayer MoS₂ severely limits its on-state C_{sc} to values well below its degenerate quantum capacitance. As a result, gate capacitance estimates made by classical equations must be corrected when evaluating the carrier density and mobility of devices with small EOTs below ~ 2 nm. Nevertheless, we find that in strong inversion, the C_G of dual-gated n -type monolayer

MoS₂ capacitors is over 50% higher than dual-gated silicon MOS capacitors at EOT = 0.5 nm and over three times higher than InGaAs capacitors at EOT = 1 nm. The monolayer MoS₂ capacitance advantage is higher at lower EOTs, ultimately indicating that strong current and transconductance may be achieved in such 2D transistors if their channel mobility and contact resistance continue to be improved.

ASSOCIATED CONTENT

Supporting Information: Description and variation of the Q-K energy valley separation; comparison to quantum capacitance approximation; methodology and results for dual-gated calculations.

Author contributions: R.K.A.B. and E.P. conceived the idea and wrote the manuscript. R.K.A.B. carried out all calculations.

Notes: The authors declare no competing financial interests.

ACKNOWLEDGMENTS

R.K.A.B. acknowledges support from the Stanford Graduate Fellowship (SGF) and the NSERC PGS-D programs. The authors also acknowledge partial support from the Stanford SystemX Alliance and from ASCENT, one of six centers in JUMP, an SRC program sponsored by DARPA.

REFERENCES

- 1 Das, S. *et al.* Transistors based on two-dimensional materials for future integrated circuits. *Nat Electronics* **4**, 786-799 (2021). DOI: 10.1038/s41928-021-00670-1
- 2 Liu, Y. *et al.* Promises and prospects of two-dimensional transistors. *Nat* **591**, 43-53 (2021). DOI: 10.1038/s41586-021-03339-z
- 3 Song, C. *et al.* Growth and Interlayer Engineering of 2D Layered Semiconductors for Future Electronics. *ACS Nano* **14**, 16266-16300 (2020). DOI: 10.1021/acsnano.0c06607
- 4 Klinkert, C. *et al.* 2-D Materials for Ultrascaled Field-Effect Transistors: One Hundred Candidates under the Ab Initio Microscope. *ACS Nano* **14**, 8605-8615 (2020). DOI: 10.1021/acsnano.0c02983
- 5 Donghyun, J., Kim, D., Taewoo, K. & Alamo, J. A. d. Quantum capacitance in scaled down III–V FETs. *2009 IEEE Int Electron Devices Meeting (IEDM)*, 1-4 (2009). DOI: 10.1109/IEDM.2009.5424312
- 6 Lundstrom, M. S. *Fundamentals of Nanotransistors* (World Scientific Publishing Company, 2017, Singapore), p. 97, 128.
- 7 Ganeriwala, M. D. *et al.* Modeling of Charge and Quantum Capacitance in Low Effective Mass III-V FinFETs. *IEEE J Electron Dev Soc* **4**, 396-401 (2016). DOI: 10.1109/JEDS.2016.2586116
- 8 Yadav, C., Ganeriwala, M. D., Mohapatra, N. R., Agarwal, A. & Chauhan, Y. S. Compact Modeling of Gate Capacitance in III–V Channel Quadruple-Gate FETs. *IEEE Trans Nanotechnol* **16**, 703-710 (2017). DOI: 10.1109/TNANO.2017.2709752
- 9 Ilatikhameneh, H. *et al.* Saving Moore’s Law Down To 1 nm Channels With Anisotropic Effective Mass. *Sci Rep* **6**, 31501 (2016). DOI: 10.1038/srep31501
- 10 Pal, H. S., Cantley, K. D., Ahmed, S. S. & Lundstrom, M. S. Influence of Bandstructure and Channel Structure on the Inversion Layer Capacitance of Silicon and GaAs MOSFETs. *IEEE Trans Electron Devices* **55**, 904-908 (2008). DOI: 10.1109/TED.2007.914830
- 11 Yoon, Y., Ganapathi, K. & Salahuddin, S. How Good Can Monolayer MoS₂ Transistors Be? *Nano Lett* **11**, 3768-3773 (2011). DOI: 10.1021/nl2018178
- 12 Ma, N. & Jena, D. Carrier statistics and quantum capacitance effects on mobility extraction in two-dimensional crystal semiconductor field-effect transistors. *2D Mater* **2**, 015003 (2015). DOI: 10.1088/2053-1583/2/1/015003
- 13 Wu, P. & Appenzeller, J. Artificial Sub-60 Millivolts/Decade Switching in a Metal–Insulator–Metal–Insulator–Semiconductor Transistor without a Ferroelectric Component. *ACS Nano* **15**, 5158-5164 (2021). DOI: 10.1021/acsnano.0c10344
- 14 Ryou, J., Kim, Y.-S., Kc, S. & Cho, K. Monolayer MoS₂ Bandgap Modulation by Dielectric Environments and Tunable Bandgap Transistors. *Sci Rep* **6**, 29184 (2016). DOI: 10.1038/srep29184
- 15 Bera, M. K. *et al.* Influence of Quantum Capacitance on Charge Carrier Density Estimation in a Nanoscale Field-Effect Transistor with a Channel Based on a Monolayer WSe₂ Two-Dimensional Crystal Semiconductor. *J Electron Mater* **48**, 3504-3513 (2019). DOI: 10.1007/s11664-019-07058-0
- 16 Rasmussen, F. A. & Thygesen, K. S. Computational 2D Materials Database: Electronic Structure of Transition-Metal Dichalcogenides and Oxides. *J Phys Chem C* **119**, 13169-13183 (2015). DOI: 10.1021/acs.jpcc.5b02950
- 17 Chen, X. *et al.* Probing the electron states and metal-insulator transition mechanisms in molybdenum disulphide vertical heterostructures. *Nat Commun* **6**, 6088 (2015). DOI: 10.1038/ncomms7088
- 18 Zhang, H., Berthod, C., Berger, H., Giamarchi, T. & Morpurgo, A. F. Band Filling and Cross Quantum Capacitance in Ion-Gated Semiconducting Transition Metal Dichalcogenide Monolayers. *Nano Lett* **19**, 8836-8845 (2019). DOI: 10.1021/acs.nanolett.9b03667
- 19 Chen, X. *et al.* Probing the electronic states and impurity effects in black phosphorus vertical heterostructures. *2D Mater* **3**, 015012 (2016). DOI: 10.1088/2053-1583/3/1/015012
- 20 Fang, N. & Nagashio, K. Quantum-mechanical effect in atomically thin MoS₂ FET. *2D Mater* **7**, 014001 (2019). DOI: 10.1088/2053-1583/ab42c0
- 21 Li, W. *et al.* Density of States and Its Local Fluctuations Determined by Capacitance of Strongly Disordered Graphene. *Sci Rep* **3**, 1772 (2013). DOI: 10.1038/srep01772

- 22 Rickhaus, P. *et al.* The electronic thickness of graphene. *Sci Adv* **6**, eaay8409
DOI: 10.1126/sciadv.aay8409
- 23 Laturia, A., Van de Put, M. L. & Vandenberghe, W. G. Dielectric properties of hexagonal boron nitride and transition metal dichalcogenides: from monolayer to bulk. *npj 2D Mater and Appl* **2**, 6 (2018).
DOI: 10.1038/s41699-018-0050-x
- 24 Lu, A. K. A., Pourtois, G., Luisier, M., Radu, I. P. & Houssa, M. On the electrostatic control achieved in transistors based on multilayered MoS₂: A first-principles study. *J Appl Phys* **121**, 044505 (2017). DOI: 10.1063/1.4974960
- 25 Fang, J., Vandenberghe, W. G. & Fischetti, M. V. Microscopic dielectric permittivities of graphene nanoribbons and graphene. *Phys Rev B* **94**, 045318 (2016). DOI: 10.1103/PhysRevB.94.045318
- 26 Giannozzi, P. *et al.* QUANTUM ESPRESSO: a modular and open-source software project for quantum simulations of materials. *J Phys Condens Mat* **21**, 395502 (2009). DOI: 10.1088/0953-8984/21/39/395502
- 27 Padilha, J. E., Peelaers, H., Janotti, A. & Van de Walle, C. G. Nature and evolution of the band-edge states in MoS₂: From monolayer to bulk. *Phys Rev B* **90**, 205420 (2014). DOI: 10.1103/PhysRevB.90.205420
- 28 Sun, X., Wang, Z., Li, Z. & Fu, Y. Q. Origin of Structural Transformation in Mono- and Bi-Layered Molybdenum Disulfide. *Sci Rep* **6**, 26666 (2016). DOI: 10.1038/srep26666
- 29 Kormányos, A. *et al.* k·p theory for two-dimensional transition metal dichalcogenide semiconductors. *2D Mater* **2**, 022001 (2015). DOI: 10.1088/2053-1583/2/2/022001
- 30 Gaddemane, G., Gopalan, S., Van de Put, M. L. & Fischetti, M. V. Limitations of ab initio methods to predict the electronic-transport properties of two-dimensional semiconductors: the computational example of 2H-phase transition metal dichalcogenides. *J Comput Electron* **20**, 49-59 (2021). DOI: 10.1007/s10825-020-01526-1
- 31 Datye, I. M. *et al.* Strain-Enhanced Mobility of Monolayer MoS₂. *Nano Lett* **22**, 8052–8059 (2022). DOI: 10.1021/acs.nanolett.2c01707
- 32 Hill, H. M., Rigosi, A. F., Rim, K. T., Flynn, G. W. & Heinz, T. F. Band Alignment in MoS₂/WS₂ Transition Metal Dichalcogenide Heterostructures Probed by Scanning Tunneling Microscopy and Spectroscopy. *Nano Lett* **16**, 4831-4837 (2016). DOI: 10.1021/acs.nanolett.6b01007
- 33 Fiore, S., Klinkert, C., Ducry, F., Backman, J. & Luisier, M. Influence of the hBN Dielectric Layers on the Quantum Transport Properties of MoS₂ Transistors. *Mater* **15** (2022). DOI: 10.3390/ma15031062
- 34 In a physical device, the remainder of the potential would be dropped across the bottom insulator, which is not observed here because we apply a Neumann boundary condition at the far side of the bottom insulator. However, we have verified that the potentials across the channel of Figure 4b,d become nearly identical to those obtained when we instead ground the far side of the bottom insulator (note that electrical ground corresponds to the mid-gap voltage) and allow the bottom insulator thickness to approach infinity.
- 35 Uchida, K. *et al.* Experimental study on carrier transport mechanism in ultrathin-body SOI nand p-MOSFETs with SOI thickness less than 5 nm. *Digest. Int Electron Devices Meeting*, 47-50 (2002). DOI: 10.1109/IEDM.2002.1175776
- 36 English, C. D., Shine, G., Dorgan, V. E., Saraswat, K. C. & Pop, E. Improved Contacts to MoS₂ Transistors by Ultra-High Vacuum Metal Deposition. *Nano Lett* **16**, 3824-3830 (2016). DOI: 10.1021/acs.nanolett.6b01309
- 37 Khan, A. I., Ashraf, M. K. & Khosru, Q. D. M. Effects of wave function penetration on gate capacitance modeling of nanoscale double gate MOSFETs. *2007 IEEE Conference on Electron Devices and Solid-State Circuits*, 137-140 (2007). DOI: 10.1109/EDSSC.2007.4450081
- 38 Yadav, C. *et al.* Capacitance Modeling in III–V FinFETs. *IEEE Trans Electron Devices* **62**, 3892-3897 (2015). DOI: 10.1109/TED.2015.2480380

Supporting Information

How do Quantum Effects Influence the Capacitance and Carrier Density of Monolayer MoS₂ Transistors?

Robert K. A. Bennett¹ and Eric Pop^{1,*}

¹Department of Electrical Engineering, Stanford University, Stanford, California 94305, U.S.A.

*Contact: epop@stanford.edu

S1. Effect of Q-K Energy Valley Separation

Our density functional theory (DFT) calculations yield an energy difference $\Delta E_{\text{QK}} \approx 0.26$ eV between the Q- and K-valleys in the conduction bands of monolayer MoS₂, as labeled in Figure S1a (we note this Q-valley is sometimes called T or Λ). However, the computed value of ΔE_{QK} for monolayer MoS₂ is highly dependent on the input parameters used in DFT (e.g., exchange-correlation functionals and pseudopotentials),¹ where the settings that yield the actual ΔE_{QK} of monolayer MoS₂ in vacuum are presently unclear. The band structure of monolayer MoS₂ also varies with the surrounding dielectric environment,² further complicating the question of which ΔE_{QK} is relevant for a given physical system.

To accommodate this uncertainty in the “correct” ΔE_{QK} , we repeat calculations of the semiconductor capacitance C_{sc} and carrier density n_{ch} for *n*-type MoS₂ with $\Delta E_{\text{QK}} = 0.13$ eV and compare these results to those obtained using $\Delta E_{\text{QK}} = 0.26$ eV in the main text. As *p*-type MoS₂ does not have an associated ΔE_{QK} or similar low-energy peaks that contribute to its density of states (DOS) in the range of energies of interest, the *p*-type results would be unchanged and are not repeated here.

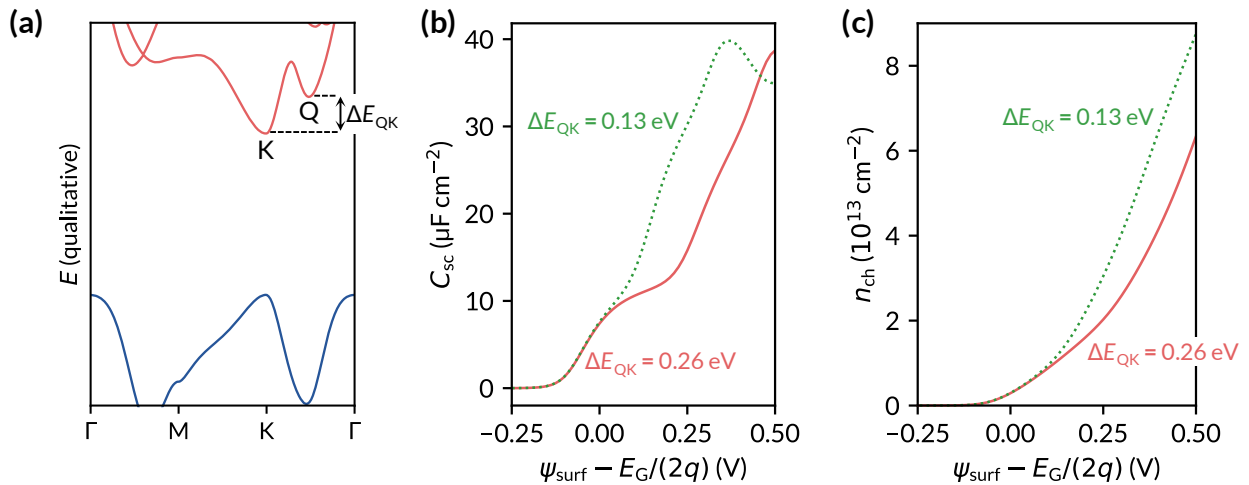


Figure S1. (a) Band structure of monolayer MoS₂ near the conduction and valence band edges obtained from DFT, where the energy separation ΔE_{QK} is labeled between the Q- and K-valleys. Energies (E) are not to scale (e.g., the band gap is reduced to highlight details of the conduction band). Note that we neglect spin-orbit coupling in this work, although for monolayer MoS₂, including spin-orbit coupling only negligibly influences the value of ΔE_{QK} obtained from DFT.¹ (b) Computed semiconductor capacitance C_{sc} and (c) carrier density n_{ch} for *n*-type monolayer MoS₂ capacitors with Q-K energy separations $\Delta E_{\text{QK}} = 0.13$ and 0.26 eV.

To obtain a local DOS (LDOS) profile with $\Delta E_{\text{QK}} = 0.13$ eV, we take the LDOS used in the main text with $\Delta E_{\text{QK}} = 0.26$ eV and splice together the LDOS at energies $E < E_C + 0.13$ eV and $E > E_C + 0.26$ eV to create a continuous LDOS profile with $\Delta E_{\text{QK}} = 0.13$ eV. We then compute C_{sc} and n_{ch} with this LDOS using the same methodology as described in the main text.

As shown in Figures S1b and S1c, C_{sc} and n_{ch} are the same for both values of ΔE_{QK} we consider at low ψ_{surf} . However, as ψ_{surf} increases, the states near the Q-valley contribute at lower energies for the LDOS profile with $\Delta E_{\text{QK}} = 0.13$ eV, resulting in an earlier onset for the second linear region of C_{sc} , thereby increasing n_{ch} . Although this lower ΔE_{QK} shifts this linear region of the C_{sc} curve to the left, it does not significantly affect the maximum value of $C_{\text{sc}} \approx 40$ $\mu\text{F}/\text{cm}^2$ in the range of ψ_{surf} we consider.

Next, we repeat the calculations of C_G and n_{ch} presented in Figures 4a,b of the main text at EOTs of 0.5, 1, and 2.5 nm using $\Delta E_{\text{QK}} = 0.13$ and 0.26 eV. As shown in Figures S2a and S2b, the value of ΔE_{QK} used affects neither C_{sc} nor n_{ch} at EOT = 2.5 nm since C_G is dominated by the oxide capacitance C_{ox} at sufficiently large EOTs. At EOT = 0.5 and 1 nm, however, we find that the higher C_{sc} at $\Delta E_{\text{QK}} = 0.13$ eV allows C_G and n_{ch} to grow closer to the classical limit compared to $\Delta E_{\text{QK}} = 0.26$ eV. This result signifies that smaller ΔE_{QK} provides further advantage of monolayer MoS₂ over Si and III-V channels from the point of view of quantum capacitance and channel carrier density at a given overdrive voltage $V_{\text{OV}} = V_G - V_T$. In practice, note that ΔE_{QK} is controlled by the strain applied³ and may be controlled by the environmental dielectric as well.

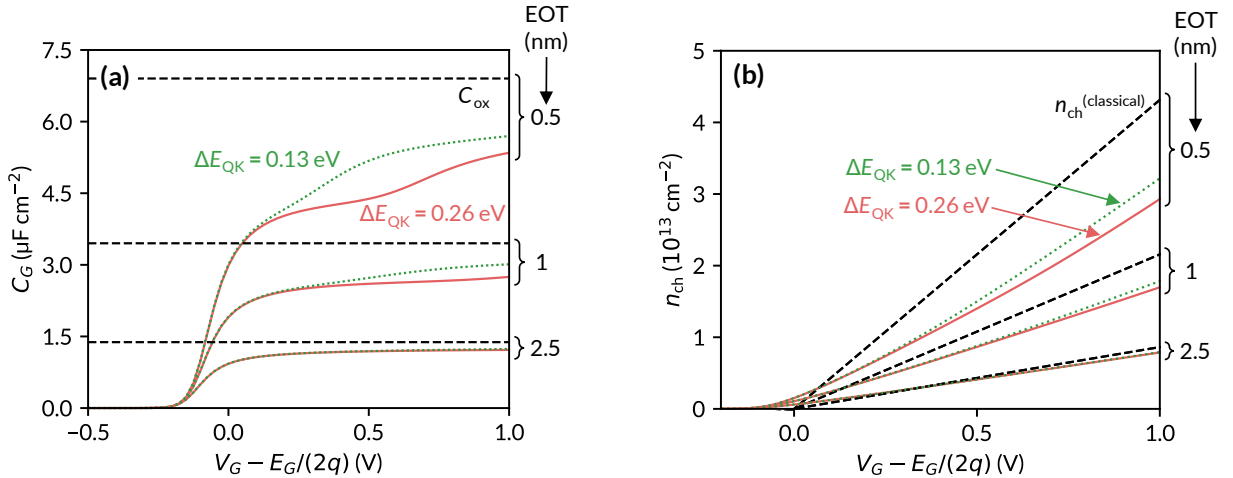


Figure S2. (a) Gate capacitance C_G and (b) carrier density n_{ch} for n -type MoS₂ with Q-K energy separations $\Delta E_{\text{QK}} = 0.13$ and 0.26 eV at EOTs of 0.5, 1, and 2.5 nm. Dotted green (solid red) lines represent the LDOS profile obtained using $\Delta E_{\text{QK}} = 0.13$ (0.26) eV. Dashed lines mark the oxide capacitance $C_{\text{ox}} = 3.9\epsilon_0/\text{EOT}$ and the conventionally calculated carrier density $n_{\text{ch}}^{\text{classical}} = C_{\text{ox}}(V_G - V_T)/q$, where the threshold voltage is $V_T = E_G/(2q)$.

S2. Comparison to Quantum Capacitance Approximation

As discussed in the main text, the classical approximation of gate capacitance, $C_G = C_{\text{ox}}$ (where C_{ox} is the oxide capacitance) and the classical approximation for charge carrier density, $n_{\text{ch}}^{\text{classical}} = C_{\text{ox}}(V_G - V_T)/q$, are well-known to be inaccurate near or below the threshold voltage V_T . Instead, C_G is typically modeled in 2D semiconductors as the series combination of the quantum capacitance C_q and the oxide capacitance C_{ox} , yielding $C_G^{-1} \approx C_{\text{ox}}^{-1} + C_q^{-1}$. Since C_q is a function of the

semiconductor's surface potential, when using this equation, C_G must be solved iteratively such that the voltage drop across the oxide and semiconductor are self-consistent with C_q . Then, n_{ch} may be approximated at any V_G by integrating this result to obtain the carrier density,

$$n_{\text{ch}}^{\text{Cq-corrected}} \approx \frac{1}{q} \int_{-E_G/2q}^{V_G} [C_q^{-1}(V'_G) + C_{\text{ox}}^{-1}]^{-1} dV'_G. \quad (\text{S1})$$

As shown in Figure S3 below, the approximation $C_G^{-1} \approx C_{\text{ox}}^{-1} + C_q^{-1}$ matches the rigorously calculated C_G presented in the main text in the subthreshold region (here $|V_G| < E_G/2q$). However, this approximation considerably overestimates the C_G of devices with $\text{EOT} \leq 1$ nm at larger overdrive voltages. This finding is consistent with our previous result from Figure 3b in the main text, which shows that C_q similarly overestimates the semiconductor's capacitance in the on-state.

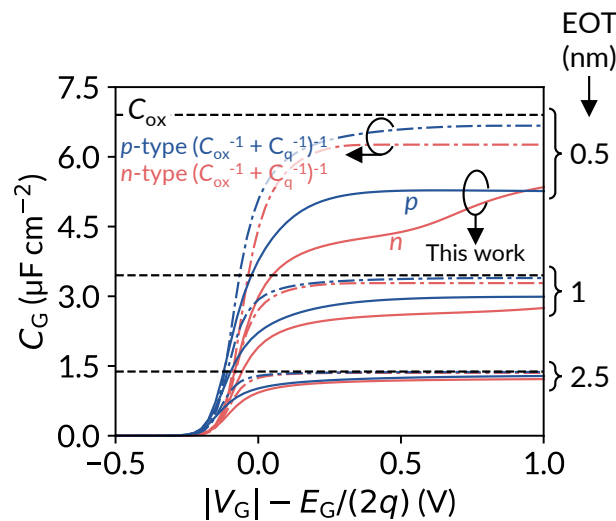


Figure S3: Gate capacitance C_G for n -type and p -type monolayer MoS_2 as functions of V_G at $\text{EOT} = 0.5, 1,$ and 2.5 nm. Solid red (blue) lines represent the C_G of n -type (p -type) MoS_2 calculated using the full *ab initio* approach described in the main text that includes charge centroid effects. Dash-dotted red (blue) lines are the approximation $C_G^{-1} \approx C_{\text{ox}}^{-1} + C_q^{-1}$ (where C_q is calculated using the self-consistent approach described above) which does not include centroid effects, and black dashed lines mark the oxide capacitance, C_{ox} . The discrepancies between solid lines and approximations highlight the importance of quantum *and* charge centroid effects in the on-state, which are most important at small EOTs.

Similarly, to compare our rigorously computed n_{ch} in the main text to the carrier density corrected with only the quantum (not centroid) capacitance, we plot our calculated n_{ch} from the main text alongside Equation S1 in Figure S4, below. For a more thorough comparison, we also include our original $n_{\text{ch}}^{\text{classical}}$ on the same plot. At an EOT of 2.5 nm, Equation S1 accurately approximates our rigorously calculated n_{ch} in both the off- and on-states. However, at $\text{EOT} = 0.5$ and 1 nm, Equation S1 does not correctly predict the charge in the on-state significantly better than the classical approximation $n_{\text{ch}}^{\text{classical}}$. Again, this result can be understood based on Figure 3b in the main text, where we show that our rigorously calculated semiconductor capacitance $C_{\text{sc}} < C_q$ in the on-state. From these results, we conclude that although including corrections for C_q enables good approximations of C_G and n_{ch} in and near the off-state, the more rigorous approach for calculating these quantities (i.e., including spatial variations in the density of states, potential, and volumetric charge density) presented in the main text should be used to understand 2D semiconductor devices with sub-1 nm EOT in the on-state.

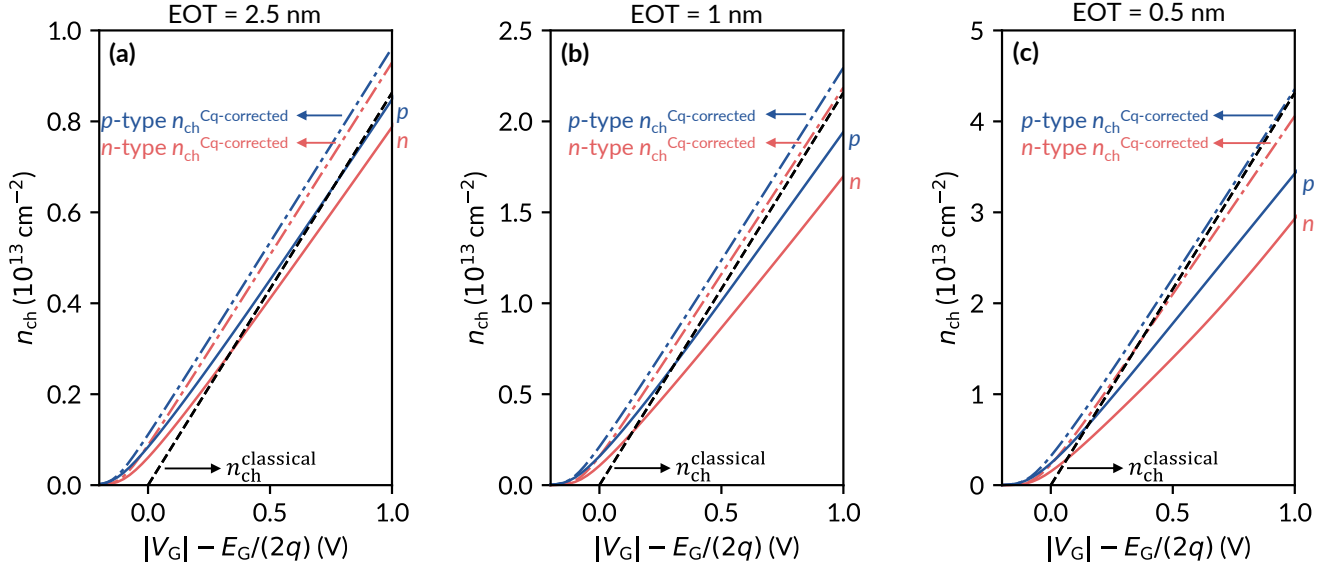


Figure S4: Charge carrier density n_{ch} for n - and p -type monolayer MoS₂ as functions of V_G at (a) EOT = 2.5 nm, (b) EOT = 1 nm, (c) EOT = 0.5 nm. Solid red (blue) lines represent n_{ch} of n - (p -) type MoS₂ calculated using the full *ab initio* approach described in the main text, which includes charge centroid effects. Dashed red (blue) lines represent the quantum capacitance-corrected carrier density $n_{\text{ch}}^{\text{Cq-corrected}}$ (Equation S1, using the self-consistent approach described above) that does not include centroid effects, and black dashed lines mark the classically calculated charge carrier density, $n_{\text{ch}}^{\text{classical}} = C_{\text{ox}}(V_G - V_T)/q$. The discrepancies between solid lines and approximations highlight the importance of quantum *and* charge centroid effects in the on-state, which are most important at small EOTs.

S3. Monolayer MoS₂ Dual-Gated Capacitors

We calculate n_{ch} and C_G of dual-gated monolayer MoS₂ capacitors by solving equations (4) and (5) in the main text self-consistently, just as we do when computing these quantities for single-gated devices. Here we use the device schematic shown in Figure S5a, which is similar to the single-gated device in Figure 1b except that the relative permittivities of both the top and bottom insulator are set to 20 and the thicknesses of the top and bottom insulators are identical. We update the bottom boundary condition [previously $\partial V(z)/\partial z = 0$ at this boundary for single-gated devices] to $V(z) = V_G$, where V_G is the gate voltage applied at both the top and bottom electrodes. We plot C_G and n_{ch} at EOT = 0.5, 1, and 2.5 nm for both n -type and p -type monolayer MoS₂ for this dual-gated device in Figures S5b,c.

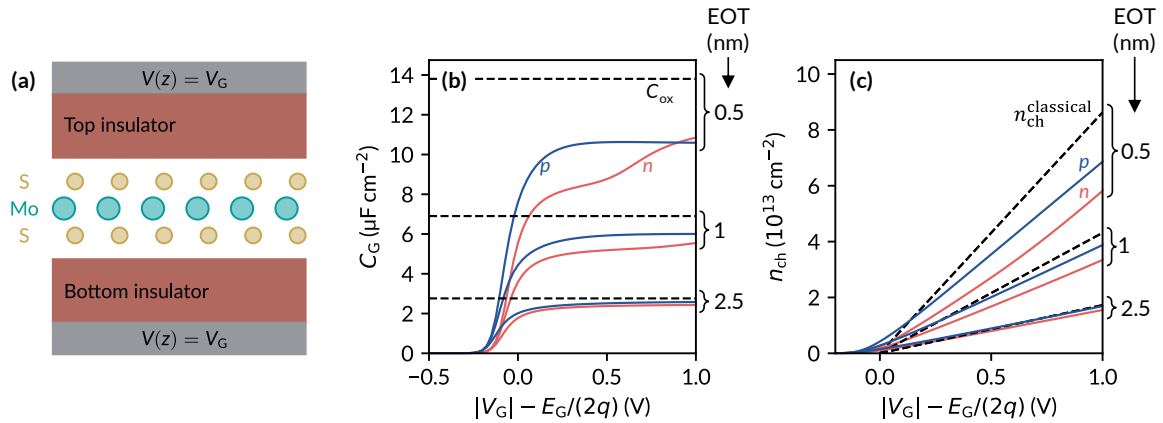


Figure S5. (a) Schematic of a monolayer MoS₂ dual-gated MOS capacitor with boundary conditions applied when solving equations (4) and (5). (b) Gate capacitance C_G and (c) carrier density n_{ch} for these dual-gated devices. Solid red (blue) lines represent n -type (p -type) MoS₂. Dashed lines mark the total dual-gated oxide capacitance $C_{ox} = 2 * (3.9\epsilon_0/EOT)$ (where the prefactor of 2 accounts for both gates) and the conventionally calculated carrier density $n_{ch}^{classical} = C_{ox}(V_G - V_T)/q$, where the threshold voltage is $V_T = \pm E_G/(2q)$ for n - and p -type devices, assuming the same gate metal.

SUPPORTING REFERENCES:

- 1 Gaddemane, G., Gopalan, S., Van de Put, M. L. & Fischetti, M. V. Limitations of ab initio methods to predict the electronic-transport properties of two-dimensional semiconductors: the computational example of 2H-phase transition metal dichalcogenides. *J Comput Electron* **20**, 49-59 (2021). DOI: 10.1007/s10825-020-01526-1
- 2 Ryou, J., Kim, Y.-S., Kc, S., & Cho, K. Monolayer MoS₂ Bandgap Modulation by Dielectric Environments and Tunable Bandgap Transistors. *Sci Rep* **6**, 29184 (2016). DOI: 10.1038/srep29184
- 3 Hosseini, M., Elahi, M., Pourfath, M., Esseni, & D. Strain induced mobility modulation in single-layer MoS₂. *J Phys D: Appl. Phys* **48**, 375104 (2015). DOI: 10.1088/0022-3727/48/37/375104